ARTICLE TYPE

Proton Conductivity in Multi-component ABO$_4$-type Oxides

Ashraf A.A. Elameen,[a,b] Arkadiusz Dawczak,[b] Tadeusz Miruszewski,[b] Maria Gazda,[b] Sebastian Wachowski[b]

This work investigates how configurational entropy in oxides could affect proton conductivity. For this purpose, three samples of different elemental compositions are synthesized. Five, six and seven elements were introduced to the A-site of the ANbO$_4$, forming La$_{1/5}$Nd$_{1/5}$Sm$_{1/5}$Gd$_{1/5}$Eu$_{1/5}$NbO$_4$, La$_{1/6}$Nd$_{1/6}$Sm$_{1/6}$Gd$_{1/6}$Eu$_{1/6}$Ho$_{1/6}$NbO$_4$ and La$_{1/7}$Nd$_{1/7}$Sm$_{1/7}$Gd$_{1/7}$Eu$_{1/7}$Ho$_{1/7}$Er$_{1/7}$NbO$_4$, respectively. The high configuration disorder changes the local environment, which can have a notable effect on many properties, including proton transport, which is the focus of this work. The conductivity was measured in different atmospheres; dry and wet and at different temperatures range ($600^\circ - 800^\circ$ C) to compare the proton transport as well as study the effect of temperature. A homogenous single-phase monoclinic fergusonite was obtained for the three samples. Proton conductivity, measured by the means of comparing of conductivity in dry and wet atmospheres, was observed in all samples. La$_{1/5}$Nd$_{1/5}$Sm$_{1/5}$Gd$_{1/5}$Eu$_{1/5}$NbO$_4$ exhibited the highest conductivity, about 3.0×10^{-6} $S.cm^{-1}$ at 800° C in the wet atmosphere, while in the dry atmosphere it was about 2.2×10^{-6} $S.cm^{-1}$ at the same temperature, which implies a modest proton conductivity in this class of materials.

1 Introduction

Multi-component materials, notably oxides, are systems where several chemical elements occupy one or more crystal sublattices, which introduces high configurational entropy. This effect can substantially change material properties. It also opens up a possibility to establish heavily doped structures, which can be used for functionally designed materials in e.g. solid state ionics. In 2015 Rost and others [1] began the work by introducing a fundamental argument about the role of configuration disorder in stabilizing High Entropy Oxides (HEOs). They studied the transition from a multi-phase system into a single phase. This was successfully verified by observing the occurrence of the minimum transition temperature at the maximum configurational entropy. Moreover, the transition was found to be endothermic. This proved that materials can be stabilized by high configurational entropy. From this point, the scientific interest in high entropy oxides sparkled [2–4]. Gazda et al. [5] focused on proton conductivity in HEOs in a work where several perovskite oxides with 5 to 7 different elements, mostly transition metals, were introduced on B-site. Some of

these perovskites, especially BaZr$_{0.2}$Sn$_{0.2}$Ti$_{0.2}$Hf$_{0.2}$Y$_{0.2}$O$_{3-\delta}$, presented substantial formation of protonic defects, thus establishing a new group of ceramic proton conductors - high entropy perovskite oxides.

Proton Conducting Ceramics (PCCs) are oxides, which at elevated temperatures conduct H^+ ions. In an oxide, a proton exists as an ionized hydrogen atom bound to an oxygen anion forming a protonic defect, which simply put is an OH^- occupying the oxygen site. Since oxides do not have protonic defects in their nominal composition the protonic defect must be formed by the exchange with the environment. In the most typical scenario protonic defects are formed via hydration reaction [6]:

$$\mathrm{v_o^{\cdot\cdot} + H_2O + O_o^x \longrightarrow 2\,OH_o^{\cdot}}$$
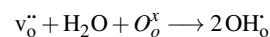
where in Kröger-Vink notation, O_o^x is a lattice Oxygen, $\mathrm{v_o^{\cdot\cdot}}$ is an Oxygen vacancy, and OH$_o^{\cdot}$ is a protonic defect.

The protons then migrate by hopping between the oxygen sites in the crystal lattice, which is often called either free proton hopping or Grotthuss mechanism [7].

PCCs gained a lot of attention over the last decades due to their possible applications in electrochemical cells, especially Proton Ceramic Fuel Cells and Steam Electrolysers, which are key elements of hydrogen technologies. More recently multiple advancements have been made both in materials research and device de-

[a] Department of Chemical and Physical Sciences, University of L'Aquila, L'Aquila, Italy
[b] Institute of Nanotechnology and Materials Engineering, Faculty of Applied Physics and Mathematics, and Advanced Materials Centre, Gdańsk University of Technology, Gdańsk, Poland

velopment. On the materials aspect, both electrolytes[8,9], which should conduct protons exclusively, and electrodes[10,11], which are mixed proton-electronic conductors, were studied. On the applications: new sustainable and fuel-flexible fuel cells[12], highly efficient steam electrolysers[13], proton ceramic reactors for direct hydrogen production from biogas, ammonia or methane[14], and proton membrane reformers for thermo-electrochemical production of hydrogen[15] were developed. This shows how important the development of PCC materials is. The ABO_4 oxides, which are the primary interest of this work, are a strong alternative for perovskite-based electrolytes. For instance, the hydration enthalpy of rare earth orthoniobates $RENbO_4$ is in the range from -115 to -165 kJ/mol[16], which makes the protonic defects more stable in these materials than in virtually any other proton conductor. As a result, in some of the $RENbO_4$ (e.g. $LaNbO_4$) compounds the protonic defects can be the dominating charge carriers up to very high temperatures, such as $900°C$, which is not observed for other PCCs. Another advantage is that there are multiple combinations of elements that can be used to form a proton conducting ABO_4 oxide. As A-site elements Y, La, Nb, Gd, Tb, Er[16] have been used, elements such as V, Nb, Ta, P, As and Sb[17] have been used on B-site. Additionally, several mixing strategies of elements on the B-site (e.g. Nb, Ta, As, Sb) have been employed to tune the functional properties such as crystal structure symmetry[18,19], thermal expansion coefficient[20], protonic defect formation[21] or conductivity[22]. This holds great promise for the potential development of high entropy derivatives of the ABO_4 oxides. The biggest disadvantage of this group is the fact that the solubility of acceptor dopants on the A-site is extremely low ($<$ 2mol. %)[23], while the B-site acceptor doping leads to the trapping of the charge carriers[24].

We believe that synthesizing a multicomponent version of ABO_4 oxide might pave the way to a new group of proton conductors. We selected $LaNbO_4$ as an acceptor doped reference material. It has the highest proton conductivity in the whole group with a maximum conductivity of 0.001 S/cm recorded at $950°C$[25]. In our approach, we decided to implement five to seven different trivalent lanthanides on the A-site of $ANbO_4$. This work shows structural and microstructural analysis of the fabricated multicomponent ABO_4 derivatives and probes the compositional effect on the proton conductivity.

2 Experimental Procedure

2.1 Synthesis

The samples will be synthesized using a multi-step solid state synthesis route. Since La_2O_3 and Nd_2O_3 are hygroscopic they will be pre-heated at $950°$ C for 12 hours with heating rate $5°C$ per minute prior to the synthesis. Then stoichiometric amounts of $La_2O_3, Nd_2O_3, Sm_2O_3, Gd_2O_3, Eu_2O_3, Ho_2O_3, Er_2O_3$ and Nb_2O_5 will be weighed. To ensure proper mixing which is essential for obtaining homogeneous multicomponent materials a multi-step route was applied. In the first step, stoichiometric amounts of precursors were weighed and mixed in an agate mortar for 30 minutes with the addition of isopropanol. The mixed powders were annealed at $750°C$ for 24 hours with a heating and cooling

rate of $5°C$ per minute. After the first step, the powders were re-mixed, sieved through 100 μm mesh and pelletized in uniaxial press under 810.0 MPa pressure. Heat treatment at the end of the second step was annealing at $1400°C$ for 12 hours with a heating and cooling rate of $2°C$ per minute. In the last stage, the samples were crushed, mixed, sieved and re-pelletized with the same conditions as in the previous step. Then they were sintered at $1500°C$ for 12 hours with a heating and cooling rate of $2°C$ per minute. In this work, three high entropy samples were prepared with three different elements contents placed in the A-site of $ANbO_4$, namely $La_{1/5}Nd_{1/5}Sm_{1/5}Gd_{1/5}Eu_{1/5}NbO_4$, $La_{1/6}Nd_{1/6}Sm_{1/6}Gd_{1/6}Eu_{1/6}Ho_{1/6}NbO_4$ and $La_{1/7}Nd_{1/7}Sm_{1/7}Gd_{1/7}Eu_{1/7}Ho_{1/7}Er_{1/7}NbO_4$. Since these materials have respectively five, six and seven elements on A-site they will be denoted as $A5NbO_4$, $A6NbO_4$ and $A7NbO_4$.

2.2 Measurements

The measurements of the structural properties were performed by X-ray diffraction powder method using Phillips X́Pert Pro diffractometer (XRD) with CuK_α (1.5418) radiation. The structural properties were refined using the Rietveld refinement method with GSASII software. The experimental data were refined by starting with $SmNbO_4$[26], with pattern number (7707609) provided at the Crystallography Open Database[27], as reference of the structure until the best fit was reached.

To study the surface morphology and the sample composition Scanning Electron Microscope(SEM) combined with Energy-dispersive X-ray spectroscopy(EDS) was used. The measurements were performed using **QUANTA FEG 250** instrument. Prior to the measurement, the samples were coated with a thin layer of Gold (3 nm) using a high vacuum sputterer **LEICA EM SCD500**. Two types of images were collected using high vacuum mode: the backscattered images and the secondary electrons images using low Voltage high Contrast Detector (vCD) and Everhart-Thornley Detector (ETD), respectively. Simultaneously, Energy-dispersive X-rays were performed in order to verify the elemental composition of the samples.

The electrical properties were investigated by the electrochemical impedance spectroscopy (EIS) technique. Prior to electrical measurements, the density of the specimen was measured by the Archimedes method using kerosene.

Two symmetrical electrodes were painted using platinum ink (ESL 5542) on both sides of the pellets. Then, the specimens were heated in the furnace at $930°C$ for three hours with a heating and cooling rate of $3°$ C. After that, the samples were measured in two atmospheres: dry, and wet air. The conditions inside the cell were controlled by a gas mixer. For dry air, the partial pressures were, $pO_2 \approx 0.2$ atm, $pH_2O \approx 10^{-5}$ atm while in wet atmosphere they were $pO_2 \approx 0.197$ atm, $pH_2O \approx 0.023$ atm. The instrument used for EIS was Gamry 3000. The spectra were collected with a voltage amplitude of 50 mV and a frequency range from 1 Hz to 1 MHz. To ensure that measurements are at thermodynamic equilibrium the impedance modulus was monitored continuously between the measurements and the spectra were collected only if it was constant.

Dilatometry measurements (DIL) were carried out with Netzsch 402 PC/4 in 50 ml/min flow of synthetic air. The heating and cooling were performed at the rate $2^{\circ}C\ min^{-1}$ from $50^{\circ}C$ to $900^{\circ}C$.

3 Results and Discussions

A single monoclinic crystal phase with a space group no 15 (I2/a) was obtained for all three materials as shown in Fig.(1)
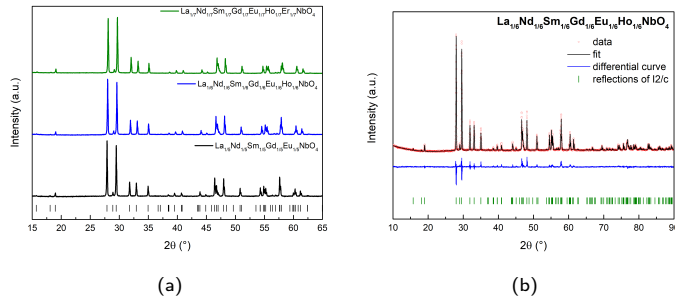

Fig. 1 XRD results for (a) the three samples: $A5NbO_4$, $A6NbO_4$ and $A7NbO_4$ (b) Rietveld refinement profile for sample $A6NbO_4$.

The findings from the refinement together are reported in Table.(1). The Goodness of Fit (GOF) representing the quality of the refinement is rather good and varies from 2.2 to 4.3. However, the difference plot shows some mismatches with respect to the intensity and width of the peaks, especially for samples $A5NbO_4$ and $A7NbO_4$. Therefore, we report only unit cell parameters obtained from the refinement. An exemplary unit cell for sample $A5NbO_4$ is shown in Fig.(2).
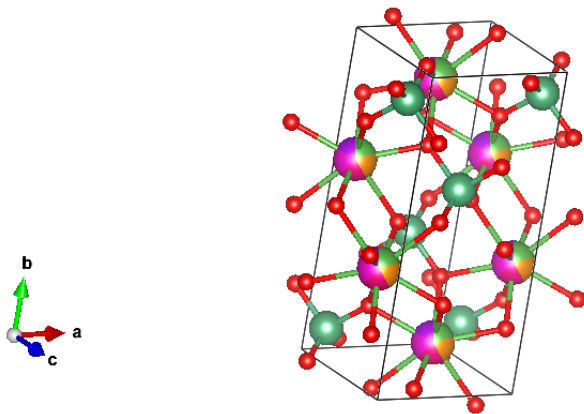

Fig. 2 The unit cell of $A5NbO_4$

One can notice that the unit cell parameters change with the number of elements on the A-site. Since with that number both the average ionic radius and entropy change it is relevant to analyse how the crystal structure evolves as a function of both parameters. To quantify the entropy we decided to use a factor called Entropy Metrics (EM), which has been introduced by Dippio and Vecchio to express the quantify high entropy materials. EM is expressed by the following formula (1) [28]:

$$S_{\text{SL}}^{\text{config}} = \frac{-R\sum_s\sum_i a^s X_i^s}{\sum_s a^s} \qquad (1)$$

where,

a^s represents the number of sites on s sublattice,

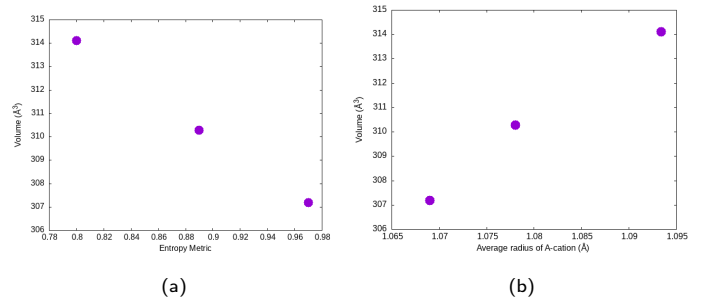X_i^s denotes the fraction of element species i distributed randomly i (s) sublattice.

Fig. 3 Unit cell volume of high entropy oxides ($A5NbO_4$, $A6NbO_4$ and $A7NbO_4$) as a function of (a) Entropy Metric and (b) the average radius of A-cation.

The unit cell volume is plotted as a function of either averaged A-site ion radius or entropy metric (EM) in Fig.(3). The volume decreases in both cases, namely when the average ionic radius decreases or EM increases. In this case it cannot be distinguished whether the entropy affects the crystal structure since it is expected that by reducing A-site ionic radius the volume would decrease [29].

The morphology and surface properties of the three samples were investigated by SEM measurements by collecting images of the backscattered electrons collected by the vCD detector. The images are shown to compare the features of the three samples together, as illustrated in Fig (4). The phase contrast of the SEM images is uniform, which reflects that the elements of the samples are uniformly distributed. Otherwise, if phase separation occurred or strong compositional inhomogeneity was present the backscattered electrons would produce an image with visible phase contrast. The overall microstructure and the morphology of all three samples are similar - a polycrystalline material with large, well-connected grains is observed. The porosity observed by SEM is similar for all specimens. This is in accordance with Archimedes' method, which yielded that all specimens have similar porosity as indicated by Table (2).
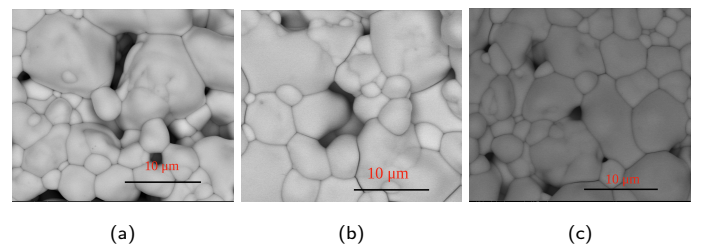

Fig. 4 Back-scattered electron micrographs of (a) $A5NbO_4$, (b) $A6NbO_4$ and (c) $A7NbO_4$.

The EDS method was employed to probe the compositions of the samples. The EDS spectra from at least three randomly selected areas were collected for each sample. An example of the spectrum is given in Fig.(5).

Table 1 Refined structural data and average radii of the A-site ions (r_A) of A5NbO$_4$, A6NbO$_4$ and A7NbO$_4$.

Material	a (Å)	b (Å)	c (Å)	β (°)	V (Å)^3	r_A(Å)	R$_{wp}$
A5NbO$_4$	5.44399(1)	11.23987(5)	5.13766(9)	94.477(9)	313.413(8)	1.0934	3.508
A6NbO$_4$	5.41861(9)	11.19152(2)	5.12675(8)	94.465(8)	309.955(4)	1.08033	3.641
A7NbO$_4$	5.39775(3)	11.15181(1)	5.1178(7)	94.463(7)	307.13(3)	1.06943	3.59

Table 2 Measured and theoretical densities and porosity of the samples.

Material	$\rho_{(Ac)}$ (g/cm^3)	$\rho_{(Th)}$ (g/cm^3)	Relative density (%)	Total porosity (%)
A5NbO$_4$	5.1(2)	6.473	78(3)	22(3)
A6NbO$_4$	5.1(2)	6.605	77(3)	23(3)
A7NbO$_4$	5.2(2)	6.715	78(3)	22(3)

Fig. 5 EDS spectra of A5NbO4 sample.

Table 3 The estimated atomic composition of A5NbO$_4$, A6NbO$_4$ and A7NbO$_4$ based on the EDS data.

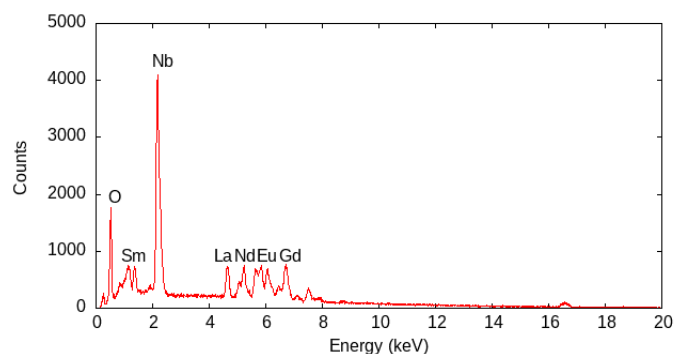| Element	A5NbO$_4$	A6NbO$_4$	A7NbO$_4$
O K	75	68	67
NbL	13(1)	16(1)	16(1)
LaL	2.5(1.0)	3.0(1.0)	2.0(1.0)
NdL	2.5(1.0)	3.0(1.0)	2.5(1.0)
SmL	2.5(1.0)	3.0(1.0)	2.5(1.0)
EuL	2.5(1.0)	3.0(1.0)	3.0(1.0)
GdL	2.5(1.0)	3.0(1.0)	2.5(1.0)
HoL	-	2.0(1.0)	2.0(1.0)
Er	-	-	2.0(1.0)

It illustrates that all elements that are expected in a given specimen are present in the spectra. Please note that we only marked the L spectral lines for all elements lanthanides and transition metals, except Sm where the M line was used. This is for the clarity of the picture since the L lines for the lanthanides overlap too much to show all the labels. Please note that the other peaks observed in the spectrum are attributed to the main specimen elements even if they are not labelled. In all selected areas the atomic composition calculated from the spectra yielded results coherent with the composition expected from the synthesis. The atomic % for each cation was within a 1 at. % margin to the values calculated from the chemical formula. The oxygen content, although given, was not analysed due to the higher uncertainty of the method for light elements. The averaged atomic composition estimated from the EDS data for each specimen is given in Table 3.

The results from Dilatometry measurements (DIL) are represented in Fig.(6). It shows the relative elongation as a function of the temperature of the A5NbO$_4$, A6NbO$_4$ and A7NbO$_4$.

All compounds show two linear regions with a transition observed around $700°C$ (marked with a vertical line in Fig.(6)). In LaNbO$_4$ and its derivatives, at the temperature where inflection appears, a structural phase transition from monoclinic $I2/a$ to
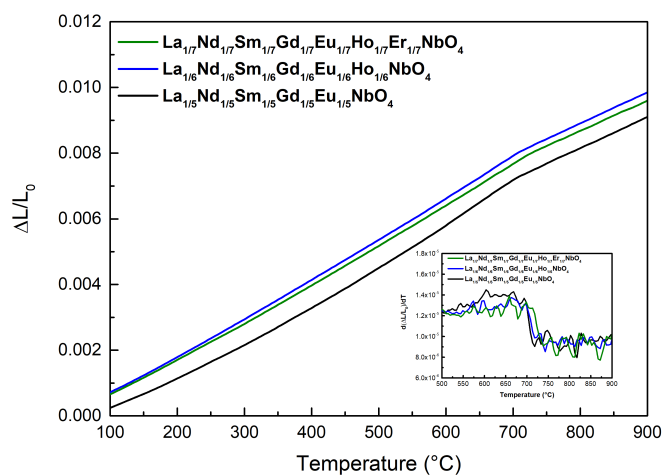

Fig. 6 Relative elongation of A5NbO$_4$, A6NbO$_4$ and A7NbO$_4$ samples as a function of the temperature. The data was recorded during cooling.

tetragonal $I41/a$ occurs[30–32]. The value of the phase transition temperature (T_0) is determined from the first derivative of the elongation function. The structural phase transition takes place in the region where the value of the first derivative changes. The temperature in the middle of that region was taken as a T_0 and the half-width of the transition range as uncertainty. Below and above the transition region the derivative is constant and represents the coefficients of linear thermal expansion (TECs) respectively for monoclinic and tetragonal phases.

Table 4 Thermal expansion coefficients and transition temperatures of the A5NbO$_4$, A6NbO$_4$ and A7NbO$_4$ materials.

Material	Thermal expansion coefficients ($10^{-6}K^{-1}$)		T_0
	Monoclinic	Tetragonal	
A5NbO$_4$	13.04 ± 0.01	9.35 ± 0.01	705 ± 7
A6NbO$_4$	12.43 ± 0.01	9.51 ± 0.01	708 ± 9
A7NbO$_4$	12.21 ± 0.01	9.23 ± 0.01	723 ± 10

The phase transition temperature slightly increases with the number of elements in the A sublattice and they are higher than LaNbO$_4$ ($500°C$[1]) and NdNbO$_4$ ($650°C$[4]), while they are lower for SmNbO$_4$ ($775°C$[5]), GdNbO$_4$ ($805°C$[6]), ErNbO$_4$ ($810°C$[7]), HoNbO$_4$ ($820°C$[7]) and EuNbO$_4$ ($830°C$[7]). As can be seen from the literature values the transition temperature decreases with increasing ionic radius of A-site cations. The trend is the same for the multicomponent oxides if the averaged ionic radius is considered. However, the slope is different and the values of transition temperatures are generally lower for multicomponent oxides than for their single A-site-cation counterparts with the same average A-site ionic radius. The phase transition in ABO$_4$ is ferroelastic, which means that spontaneous strain is present in the monoclinic phase and it diminishes upon transition to tetragonal polymorph[30]. We have shown that chemical composition influences the spontaneous strain present in the monoclinic phase and it is related to the phase transition temperature[33]. We believe that also in this case, the presence of multiple components on the A-site will affect the strain in the crystal lattice and in turn, will change the phase transition temperature. Under $700°C$, in conditions where the material is monoclinic TECs are decreasing with the increase of the number of elements in A sublattice. What is interesting, NdNbO$_4$ and SmNbO$_4$ have quite similar values of TECs such as $12.8 \times 10^{-6}K^{-1}$ and $11.4 \times 10^{-6}K^{-1}$, respectively[32]. While above $700°C$, in the tetragonal phase, the TECs values do not show a clear trend with respect to the number of elements in the A-site. TECs for the tetragonal phase are of similar value to other tetragonal ABO$_4$ oxides (approx. $10 \times 10^{-6}K^{-1}$)[32]. In Fig.(7) the phase transition temperatures as a function of averaged A-site ion radius of the A5NbO$_4$, A6NbO$_4$ and A7NbO$_4$ samples are plotted. For comparison, the phase transformation temperatures of EuNbO$_4$, SmNbO$_4$ and NdNbO$_4$ are shown since, as these oxides have similar A-site ionic radius to the averaged values of the studied HEOs. The dashed dot lines are added to provide guidance for the eye. As can be seen, the tow entropy materials (EuNbO$_4$, SmNbO$_4$ and NdNbO$_4$) show much steeper change of transition temperature with the change of ionic radius than in the case of the multicomponent oxides.
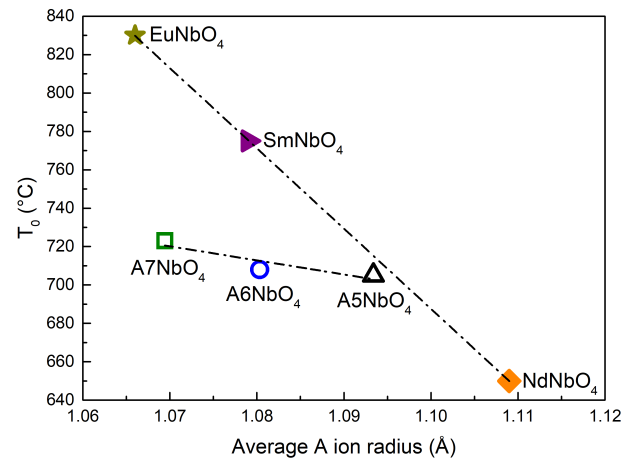

Fig. 7 Phase transition temperature as a function of average ionic radius for the A sublattice of the A5NbO$_4$, A6NbO$_4$ and A7NbO$_4$ materials (hollow marks). In addition, the phase transition temperatures of some rare-earth ortho-niobates (filled marks), with similar A-site element ionic radii to the averaged ionic radii of our compounds, are presented. The reference values are taken from[29,34–36].

To evaluate the electrical properties of studied materials, Electrochemical Impedance Spectroscopy (EIS) measurements as a function of temperature have been performed. An example of a complex impedance plot was shown Fig.(8). In Fig.(8), each
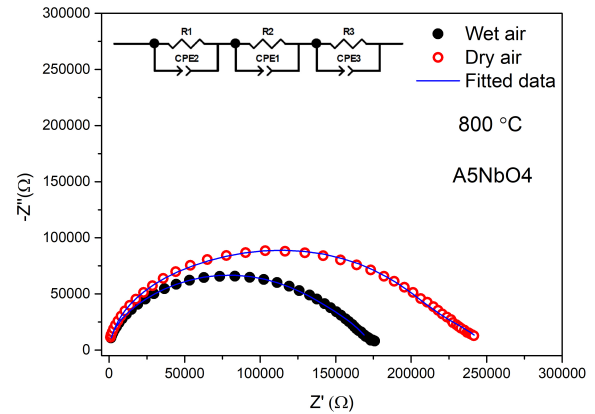

Fig. 8 Nyquist plot with the corresponding fit (solid line) for A5NbO4 sample collected in both dry and wet air at $800°C$.

semicircle is represented by an element (RQ), where R refers to the resistance of material and Q represents a pseudocapacitance of a constant phase element. Identification of which electrochemical processes were represented by each semicircle in the EIS spectra was performed on the base of capacitance responses, and analyzed in ZView software[37].

The capacitance C_{geom} in relation to the geometry of sample for each (RQ) circuit was calculated using the following formulas:

$$C = Q^{\frac{1}{n}} R^{\frac{1}{n}-1} \tag{2}$$

$$C_{\text{geom}} = C\frac{1}{S} \qquad (3)$$

where C is a capacitance, Q denotes a pseudocapacitance obtained by a fitting of a suitable model shown in Fig.(8), R is the resistance of the material, l is the length of the pellet, and S is the area of the platinum electrode. The C_{geom} responses were in the order of 10^{-12} - $10^{-9} F*cm^{-1}$, thus it was considered as a bulk response. Interestingly, no response was observed from the electrode processes, which typically have capacitances of $10^{-7} - 10^{-5} F/cm$, which means that the kinetics of the charge transfer on the electrodes was relatively high[38]. All resistance and capacitance parameters obtained as a result of the impedance spectra fit are presented in the Supplementary Material. The total conductivity σ_{tot}, which is a sum of grain and grain boundaries conductivity, was calculated by using Eq.(4)

$$\sigma_{\text{tot}} = \frac{1}{R_{\text{tot}}} \cdot \frac{1}{S} \qquad (4)$$

where R_{tot} is the total resistance of the material, estimated from the fitting of impedance spectra (see Fig.(8)). The temperature-dependence of total electrical conductivity was plotted from $600°C$ to $800°C$ for A5NbO$_4$, A6NbO$_4$ and A7NbO$_4$ samples, and was shown in Fig.(9), Fig.(10) and Fig.(11).

Fig. 10 Total electrical conductivity for A6NbO$_4$ as a function of temperature, measured in dry air ($pH_2O \approx 10^{-5}$ $atm.$) and wet air ($pH_2O \approx 0.023$ $atm.$).
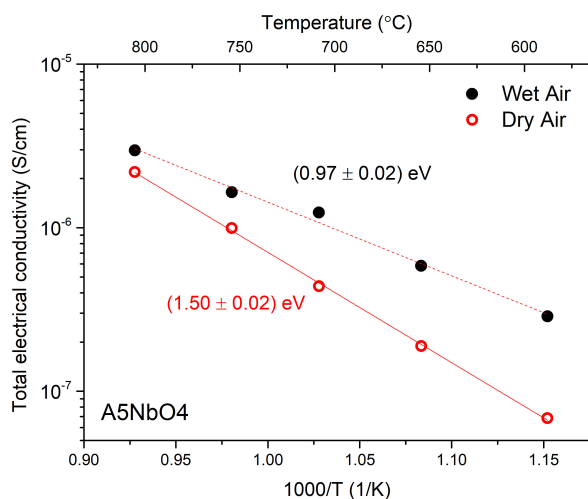

Fig. 9 Total electrical conductivity for A5NbO$_4$ as a function of temperature, measured in dry air ($pH_2O \approx 10^{-5}$ $atm.$) and wet air ($pH_2O \approx 0.023$ $atm.$)

As can be seen, A5NbO$_4$, A6NbO$_4$ and A7NbO$_4$ samples exhibit thermally activated character of electrical conductivity. The reported conductivities for the highest measured temperature, $800°C$, in both wet and dry conditions, were in the order of $10^{-6} S/cm$ for all samples. The recorded conductivities at the lowest measured temperature - $600°C$ - were in the range of $10^{-7} S/cm$. Nevertheless, the conductivity values in the wet atmosphere were higher than those in the dry atmosphere, but the difference did not differ by one order of magnitude. These values are lower than the recorded values of some PCCs. For examples, $BaZr_{0.85}Y_{0.15}O_3$ exhibited $1.8 \times 10^{-3} S/cm$ at $350°C$, $Ba_{0.97}Zr_{0.77}Y_{0.19}Zn_{0.04}O_3$ showed $1.7 \times 10^{-5} S/cm$ at $300°C$ and
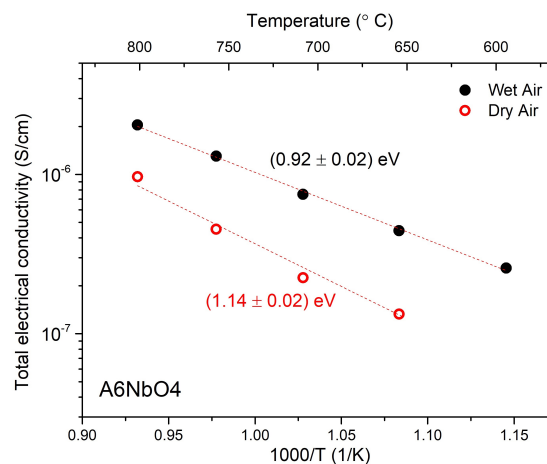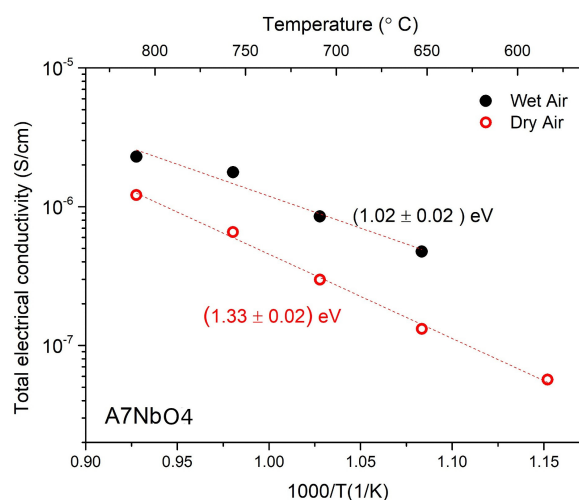

Fig. 11 Total electrical conductivity for A7NbO$_4$ as a function of temperature, measured in dry air ($pH_2O \approx 10^{-5}$ $atm.$) and wet air ($pH_2O \approx 0.023$ $atm.$).

most recently Ba_2LuAlO_5 recorded conductivity of $10^{-2}S/cm$ at $487°C$[39,40]. This is lower than expected change, but it can be still related to the hydration of doped A5NbO$_4$ under humidified atmospheres[25,41]. The observed difference is the biggest at lower temperatures and decreases with increasing temperature, which is due to the higher proton concentration at lower temperatures. It was previously observed in acceptor-doped lanthanum orthoniobate by many research groups[42,43]. Moreover, no significant trends of changes in the electrical conductivity values at the same temperature (for example, $700°C$) were observed as a function of the number of components in the A-sublattice of lanthanum orthoniobate. The observed impact is rather indirect. The introduction of many cations with different average ionic radii into the oxide structure results in structural distortions, caused by the atomic-size mismatch. This can have an impact on both electronic and ionic transport. The LaNbO$_4$-based compound studied in this work shows mainly the electrical conductivity of oxygen ions and protonic defects in measurement atmospheres. The hopping mechanism of these charge carriers depends, among others, on the distance between oxygen ions in neighbouring unit cells, which may differ significantly due to lattice distortion. Therefore, it could slow the diffusion of the protons/oxygen ions and therefore lower the total electrical conductivity. The influence of the presence of many cations in the structure of oxides has been studied in the literature, where, as in this work, a decrease in electrical conductivity was noticed due to the presence of many cation[44,44,45]. Moreover, many acceptor-type cations in the structure bring more oxygen vacancies, which later contribute to the formation of protonic defects in a wet atmosphere. However, it hinders the mobility of the protons which results in a lower electrical conductivity as reported in this work[44,46–48]. In multi-component lanthanum orthoniobate substituted with many cations in sublattice A, the electric charge transport has not yet been studied and published in the literature. In this work, we observed, that the level of total electrical conductivity of all three measured compositions is less than one order of magnitude lower than that of pure, unsubstituted LaNbO$_4$ ($\sim 2.0 \times 10^{-5}S/cm$ at $700°C$ measured in wet air[49]). Thus, it can be seen that the introduction of many cations into the A sublattice resulted in a decrease in electrical conductivity, which may be caused by both a decrease in the concentration of charge carriers and their mobility, resulting from the distortion of the crystal structure. Determining the impact of structural distortions in multi-component materials based on LaNbO$_4$ separately on concentration and separately on mobility requires additional research. To estimate the activation energy of the conduction mechanism for each sample, total electrical conductivity data shown in Fig.(9), Fig.(10) and Fig.(11) was fitted to Eq.(5):

$$\sigma = \frac{\sigma_0}{T} e^{-\frac{E_A}{kT}} \tag{5}$$

where E_A is the apparent activation energy of the thermally activated hopping mechanism, T denotes an absolute temperature, σ_0 is a pre-exponential factor and k is a Boltzmann constant. The activation energy for three samples in both dry and wet atmospheres are listed in Table (5)

Table 5 The activation energy for conduction mechanism, estimated for A5NbO$_4$, A6NbO$_4$ and A7NbO$_4$ in wet and dry conditions.

Material	$E_A \pm 0.02$ (Wet) (eV)	$E_A \pm 0.02$ (Dry) (eV)
A5NbO$_4$	1.00	1.50
A6NbO$_4$	0.92	1.14
A7NbO$_4$	1.02	1.33

The energy values in the dry air range from 1.1 to 1.5 eV, while those determined for the wet air atmosphere are lower for each of the three samples and have been estimated to be $0.9 - 1.0$ eV, depending on the sample. The lowest activation energy in dry air - 1.14 ± 0.02 eV – was observed in a sample containing 6 elements in the lanthanum sublattice, while the highest of 1.50 ± 0.02 eV is found in the case of the A5NbO$_4$ sample. In wet air, the activation energies are very comparable for the 3 samples, the changes being less than 10%. It is interesting that the activation energy values obtained from measurements in wet air are much lower than those for undoped LaNbO4, measured in similar gas conditions. Cao et al. [50] obtained a value of about 1.5 eV for pure lanthanum orthoniobate in the monoclinic structure temperature range, while in the present work, all 3 samples showed an activation energy of around 1.0 eV. It is also interesting, that the conductivity level turned out to be lower than that of pure LaNbO$_4$ for both atmospheres, while the activation energy was lower by 0.5 eV than the value for LaNbO$_4$. This may be due to the fact that in the case of significant structural distortions, the concentration and mobility of mobile ionic species (protons and oxygen vacancies) are lower, while the enthalpy of mobility can be lower. In multicomponent oxides, the disordering of the crystal lattice may highly hinder proton mobility by altering the O-H bond length as well as the possible minimum energy paths. It was also observed, that in the whole range of measured temperatures, one activation energy was obtained. A fit of Eq.(5) for experimental data shown in Fig.(9), Fig.(10) and Fig.(11) in the whole temperature range was good ($R^2 > 0.99$). There is no visible change in electrical properties (activation energy) above the temperature of phase transitions from monoclinic to tetragonal ($\sim 700°C$). The phase transition was clearly visible in this work in the dilatometry results around $700°C$ for all samples (see Fig.(6)), but it had no significant effect on the transport of charge carriers. For example, in Mg or Ca-doped LaNbO$_4$ in the amount of 2mol%, where the change in the slope of the curve in the conductivity graph in Arrhenius coordinates around the phase transition temperature ($\sim 530°C$[50,51]) is clearly visible. In the case of samples examined in this work, containing as many as 5 cations in the lanthanum sublattice, this type of transition was not observed in electrical studies.

4 Summary and conclusions

The single-phase, homogenous La$_{1/5}$Nd$_{1/5}$Sm$_{1/5}$Gd$_{1/5}$Eu$_{1/5}$NbO$_4$, La$_{1/6}$Nd$_{1/6}$Sm$_{1/6}$Gd$_{1/6}$Eu$_{1/6}$Ho$_{1/6}$NbO$_4$ and La$_{1/7}$Nd$_{1/7}$Sm$_{1/7}$Gd$_{1/7}$Eu$_{1/7}$Ho$_{1/7}$Er$_{1/7}$NbO$_4$ orthoniobates were obtained by solid state synthesis. At room temperature, for all three compounds, a monoclinic fergusonite structure was

observed. The Rietveld analysis showed that unit cell volume decreased with decreasing average A-cation radius whereas the monoclinic angle remained constant 94.46°.

Thermal studies, conducted by dilatometry measurements, revealed a phase transition in a temperature range of $700 - 720°$ C, which is much higher than that of $LaNbO_4$ and lower than these of e.g. $SmNO_4$, $GdNbO_4$ and $EuNbO_4$. What we consider very interesting, the transition temperature dependence on the average A-cation radius in the multicomponent orthoniobates is much weaker in comparison to the single A-cation compounds ($EuNbO_4$, $SmNbO_4$ and $NdNbO_4$).

The studies of electrical properties in dry and wet air showed, that the total electrical conductivity of all three compounds is described by a lower activation energy lower value than that of $LaNbO_4$. This could be attributed to the disordering of the crystal lattice due to the presence of many cations in La-site. The measurements of conductivity in both dry and wet air atmospheres revealed the possibility of proton conductivity in such a class of materials.

Acknowledgements

Notes and references

1 C. M. Rost, *Nature Communications*, 2015, **6**, 1–8.

2 C. Oses, C. Toher and S. Curtarolo, *Nature Reviews Materials*, 2020, **5**, 295–309.

3 S. Akrami, P. Edalati, M. Fuji and K. Edalati, *Materials Science and Engineering: R: Reports*, 2021, **146**, 100644.

4 H. Xiang, Y. Xing, F.-z. Dai, H. Wang, L. Su, L. Miao, G. Zhang, Y. Wang, X. Qi, L. Yao *et al.*, *Journal of Advanced Ceramics*, 2021, **10**, 385–441.

5 M. Gazda, T. Miruszewski, D. Jaworski, M.-G. A. leksandra, W. Skubida, S. Wachowski, P. Winiarz, K. Dzierzgowski, M. Łapinski, I. Szpunar *et al.*, *ACS Materials Letters*, 2020, **2**, 1315–1321.

6 M. Marrony, *Proton-conducting ceramics: from fundamentals to applied research*, CRC Press, 2015.

7 K.-D. Kreuer, A. Fuchs and J. Maier, *Solid State Ionics*, 1995, **77**, 157–162.

8 J. Tong, D. Clark, L. Bernau, M. Sanders and R. O'Hayre, *Journal of Materials Chemistry*, 2010, **20**, 6333–6341.

9 Z. Zhong, Z. Li, J. Li, X. Guo, Q. Hu, Y. Feng and H. Sun, *International Journal of Hydrogen Energy*, 2022, **47**, 40054–40066.

10 R. Merkle, M. F. Hoedl, G. Raimondi, R. Zohourian and J. Maier, *Annual Review of Materials Research*, 2021, **51**, 461–493.

11 S. L. Wachowski, I. Szpunar, M. H. Sørby, A. Mielewczyk-Gryń, M. Balaguer, C. Ghica, M. C. Istrate, M. Gazda, A. E. Gunnæs, J. M. Serra *et al.*, *Acta Materialia*, 2020, **199**, 297–310.

12 C. Duan, J. Tong, M. Shang, S. Nikodemski, M. Sanders, S. Ricote, A. Almansoori and R. O'Hayre, *Science*, 2015, **349**, 1321–1326.

13 E. Vøllestad, R. Strandbakke, M. Tarach, D. Catalán-Martínez, M.-L. Fontaine, D. Beeaff, D. R. Clark, J. M. Serra and T. Norby, *Nature materials*, 2019, **18**, 752–759.

14 D. Clark, H. Malerød-Fjeld, M. Budd, I. Yuste-Tirados, D. Beeaff, S. Aamodt, K. Nguyen, L. Ansaloni, T. Peters, P. K. Vestre *et al.*, *Science*, 2022, **376**, 390–393.

15 H. Malerød-Fjeld, D. Clark, I. Yuste-Tirados, R. Zanón, D. Catalán-Martinez, D. Beeaff, S. H. Morejudo, P. K. Vestre, T. Norby, R. Haugsrud *et al.*, *Nature Energy*, 2017, **2**, 923–931.

16 R. Haugsrud and T. Norby, *Nature Materials*, 2006, **5**, 193–196.

17 P. Winiarz, K. Dzierzgowski, A. Mielewczyk-Gryń, M. Gazda and S. Wachowski, *Chemistry–A European Journal*, 2021, **27**, 5393–5398.

18 S. Wachowski, B. Kamecki, P. Winiarz, K. Dzierzgowski, A. Mielewczyk-Gryń and M. Gazda, *Inorganic Chemistry Frontiers*, 2018, **5**, 2157–2166.

19 S. L. Wachowski, B. Kamecki, P. Winiarz, K. Dzierzgowski, M. Jurkowski, J. Dzisevič, A. Mielewczyk-Gryń and M. Gazda, *ChemistrySelect*, 2019, **4**, 8645–8651.

20 S. Wachowski, A. Mielewczyk-Gryn and M. Gazda, *Journal of Solid State Chemistry*, 2014, **219**, 201–209.

21 A. Mielewczyk-Gryń, S. Wachowski, M. Prześniak-Welenc, K. Dzierzgowski, A. Regoutz, D. J. Payne and M. Gazda, *Journal of Thermal Analysis and Calorimetry*, 2019, **138**, 225–232.

22 S. Wachowski, A. Mielewczyk-Gryń, K. Zagórski, C. Li, P. Jasiński, S. J. Skinner, R. Haugsrud and M. Gazda, *Journal of Materials Chemistry A*, 2016, **4**, 11696–11707.

23 T. Mokkelbost, H. L. Lein, P. E. Vullum, R. Holmestad, T. Grande and M.-A. Einarsrud, *Ceramics International*, 2009, **35**, 2877–2883.

24 M. Huse, T. Norby and R. Haugsrud, *International journal of hydrogen energy*, 2012, **37**, 8004–8016.

25 R. Haugsrud and T. Norby, *Solid State Ionics*, 2006, **177**, 1129–1135.

26 B. G. Mullens, M. Avdeev, H. E. Brand, S. Mondal, G. Vaitheeswaran and B. J. Kennedy, *Dalton Transactions*, 2021, **50**, 9103–9117.

27 A. Vaitkus, A. Merkys and S. Gražulis, *Journal of applied crystallography*, 2021, **54**, 661–672.

28 D. B. Miracle and O. N. Senkov, *Acta Materialia*, 2017, **122**, 448–511.

29 S. W. Arulnesan, P. Kayser, J. A. Kimpton and B. J. Kennedy, *Journal of Solid State Chemistry*, 2019, **277**, 229–239.

30 L. Jian and C. Wayman, *Journal of the American Ceramic Society*, 1997, **80**, 803–806.

31 L. Hakimova, A. Kasyanova, A. Farlenkov, J. Lyagaeva, D. Medvedev, A. Demin and P. Tsiakaras, *Ceramics International*, 2019, **45**, 209–215.

32 P. Zhang, Y. Feng, Y. Li, W. Pan, P.-a. Zong, M. Huang, Y. Han, Z. Yang, H. Chen, Q. Gong *et al.*, *Scripta Materialia*, 2020, **180**, 51–56.

33   A. Mielewczyk-Gryn, S. Wachowski, K. Lilova, X. Guo, M. Gazda and A. Navrotsky, *Ceramics International*, 2015, **41**, 2128–2133.

34   M. Saura-Múzquiz, B. G. Mullens, H. E. Maynard-Casely and B. J. Kennedy, *Dalton Transactions*, 2021, **50**, 11485–11497.

35   O. Kondrat'eva, G. Nikiforova, A. Tyurin, A. Khoroshilov, V. Gurevich and K. Gavrichev, *Journal of Alloys and Compounds*, 2019, **779**, 660–666.

36   L. Kukueva, L. Ivanova and Y. N. Venevtsev, *Ferroelectrics*, 1984, **55**, 129–133.

37   D. Johnson, *Scribner Associates Inc., Southern Pines*, 1990.

38   J. T. Irvine, D. C. Sinclair and A. R. West, *Advanced materials*, 1990, **2**, 132–138.

39   Y. Meng, J. Gao, Z. Zhao, J. Amoroso, J. Tong and K. S. Brinkman, *Journal of Materials Science*, 2019, **54**, 9291–9312.

40   R. Morikawa, T. Murakami, K. Fujii, M. Avdeev, Y. Ikeda, Y. Nambu and M. Yashima, *Communications Materials*, 2023, **4**, 42.

41   L. E. Rohde, N. Clausell, J. P. Ribeiro, L. Goldraich, R. Netto, G. W. Dec, T. G. DiSalvo and C. A. Polanczyk, *International journal of cardiology*, 2005, **102**, 71–77.

42   Z. Bi, C. A. Bridges, J.-H. Kim, A. Huq and M. P. Paranthaman, *Journal of Power Sources*, 2011, **196**, 7395–7403.

43   T. S. Bjørheim, T. Norby and R. Haugsrud, *Journal of Materials Chemistry*, 2012, **22**, 1652–1661.

44   Y. Shi, N. Ni, Q. Ding and X. Zhao, *Journal of Materials Chemistry A*, 2022, **10**, 2256–2270.

45   P. Vanitha, A. Arulraj, P. Santhosh and C. Rao, *Chemistry of materials*, 2000, **12**, 1666–1670.

46   Q. Yang, G. Wang, H. Wu, B. A. Beshiwork, D. Tian, S. Zhu, Y. Yang, X. Lu, Y. Ding, Y. Ling *et al.*, *Journal of Alloys and Compounds*, 2021, **872**, 159633.

47   Y. Zheng, M. Zou, W. Zhang, D. Yi, J. Lan, C.-W. Nan and Y.-H. Lin, *Journal of Advanced Ceramics*, 2021, **10**, 377–384.

48   Y. Ma, Y. Chen, M. Sun and Y. Zhang, *The Chemical Record*, 2022, e202200195.

49   K. Dzierzgowski, S. Wachowski, M. Łapiński, A. Mielewczyk-Gryń and M. Gazda, *Materials*, 2022, **15**, 2267.

50   Y. Cao, N. Duan, D. Yan, B. Chi, J. Pu and L. Jian, *International journal of hydrogen energy*, 2016, **41**, 20633–20639.

51   A. Mielewczyk-Gryn, K. Gdula-Kasica, B. Kusz and M. Gazda, *Ceramics International*, 2013, **39**, 4239–4244.